Research Article Vol. 42, No. 11 / November 2025 / Journal of the Optical Society of America B 2369

Journal of the Optical Society of America B

OPTICAL PHYSICS

Wavelength-scalable mid-infrared photodetectors based on photon-assisted tunneling in MIM metasurfaces

PARHAM HEIDARZADEH,[1] JIMMY CHING-MING CHEN,[2] ZHIXIAN ZHOU,[3] AND PAI-YEN CHEN[1,*]

[1]Department of Electrical and Computer Engineering, University of Illinois at Chicago, Chicago, Illinois 60607, USA
[2]Department of Engineering Technology, Wayne State University, Detroit, Michigan 48202, USA
[3]Department of Physics and Astronomy, Wayne State University, Detroit, Michigan 48201, USA
*pychen@uic.edu

Received 25 June 2025; revised 29 August 2025; accepted 15 September 2025; posted 16 September 2025; published 2 October 2025

We propose zero-bias, wavelength-scalable, and polarization-selective mid-infrared photodetectors based on metal–insulator–metal (MIM) metasurfaces. Specifically, these photodetectors leverage the second-order quantum conductivity sourced from photon-assisted tunneling and strong electric field localization in the MIM nanojunction to achieve efficient optical rectification. We show that by tailoring metasurface geometry, the incident infrared radiation can be efficiently coupled into the MIM heterojunction, with certain wavelength and polarization selectivity, and the optical rectification effect can be achieved with a photoresponsivity as high as tens of mA/W. Such results may pave a promising route toward the next-generation mid-infrared photodetection and energy harvesting.

https://doi.org/10.1364/JOSAB.571626

1. INTRODUCTION

Mid-infrared (MIR) photodetection has many scientific and technological applications, including thermal imaging, environmental monitoring, molecular spectroscopy, free-space optical communication, biomedical sensing, and atmospheric sensing that relies on MIR detection for the determination of the composition of gases based on their absorption fingerprints [1,2]. However, conventional infrared photodetectors based on narrow-bandgap semiconductors generally suffer from inherent limitations, such as frequent Auger recombination and the need for cryogenic cooling, which, although effective in suppressing thermal noise, make the devices bulky and cumbersome [3]. Therefore, there is an urgent need for the development of compact MIR photodetectors that do not require cryogenic cooling and can efficiently couple light into the device and generate detectable photocurrents. In the near-infrared (NIR) and visible range, hot-electron photodetectors based on plasmonic nanoantennas have been demonstrated to be effective sub-bandgap and wavelength-selective photodetectors [4–6]. These devices leverage the wavelength/polarization-selective resonant excitation of plasmons and hot electron injection (internal photoemission) in the metal–insulator–metal (MIM) or metal–semiconductor heterostructures to generate photocurrents and achieve sub-bandgap photodetection in the NIR and visible range [7]. In the long-wavelength region, photolithographically fabricated microantennas loaded with an MIM diode have been exploited to couple far-infrared (FIR) radiation into the MIM heterojunction to generate photocurrents through the ultrafast rectification effect [8]. By appropriately designing the geometry of a micromachined antenna, broadband or spectrally selective FIR photodetection can be achieved [9–12]. Although such optical rectifying antennas (or rectennas) allow for sub-bandgap photodetection in the long-wavelength region, they generally suffer from low responsivity due to challenges in impedance matching between the antenna and the input impedance of the diode (which includes the dynamic resistance and the large parasitic capacitance), the relatively small reception areas, and rather complicated interconnect and bias circuitry.

Plasmonic metamaterials and metasurfaces are emerging as promising nanophotonic and nano-optical devices for controlling and manipulating light scattering and absorption at the nanoscale. When they are irradiated by light, the resonant excitation of surface plasmon polaritons can lead to significant optical extinction and field localization in the proximity of a meta-atom constituting the metamaterial or metasurface [13]. Strong light–matter interactions have been shown to confine optical fields into a subdiffractional hot spot [14,15]. In this regard, plasmonic metasurfaces have been proposed to enhance the intrinsically weak nonlinear responses of second or third order of optical materials [16–18]. By properly patterning the MIM heterojunction into the metasurface structure, a huge

local field enhancement, which increases as the feed gap is downscaled, can be achieved to augment the nonlinear optical effects. Moreover, when the nanogap of an MIM heterojunction is sufficiently small (i.e., nanometer/sub-nanometer scale), tunneling of plasmons can be driven by electromagnetic fields [19–21] and, thus, photon-assisted tunneling emerges inevitably, giving rise to conduction currents at the fundamental frequency and its high harmonics, which in turn lead to versatile nonlinear optical and optoelectronic phenomena, such as second-harmonic generation and optical rectification. In this work, we further put forward the idea of using an MIM metasurface to enhance the second-order quantum conductivity occurring in the MIM heterojunction, to enable the efficient optical rectification effect and the sub-bandgap photodetection in the MIR range. We theoretically demonstrate several sub-bandgap MIR photodetectors based on MIM metasurfaces, which allow for enhanced light absorption, spectral tunability, and polarization selectivity. In the following, we will present zero-bias MIM photodetectors that achieve responsivity of the order of 10 mA/W in the MIR region, with wavelength and polarization dependencies. Additionally, we will show that the operating spectral range can be broadened by designing a multi-resonance MIM metasurface in the MIR region.

2. MULTIPHOTON-ASSISTED QUANTUM TUNNELING

In recent years, semiclassical and quantum-corrected models based on the multiphoton-assisted tunneling theorem have been proposed to study localized and tunneling plasmons inside a nanojunction. More recently, on-chip tunneling-based light emission has been introduced through plasmonic metasurfaces, integrating quantum tunnel junctions, which shows that inelastic electron tunneling can behave as both the excitation source and the sensing mechanism in nanoscale biosensors [20]. Alongside these advances, harmonic nanoantennas have been theoretically shown to use photon-assisted tunneling to achieve second-harmonic generation, where the nonlinear conductance in dissimilar MIM nanogaps depends on the electronic affinity and permittivity of molecular loads, which enables background-free molecular identification through their second-harmonic response [21]. In addition, intense localized electric fields in plasmonic nanogaps have been shown to result in nonlinear tunneling processes and multiphoton transitions, establishing a connection between photon-assisted tunneling and surface plasmon excitations [4,22]. Experimental works on nonadiabatic nano-optical tunneling have shown that few-cycle plasmonic near-fields are able to drive photoelectron emission beyond conventional dynamics [23]. Furthermore, a density-matrix approach shows photon-assisted tunneling as the leading term and higher-order multiphoton currents, with confined optical fields in MIM gaps mapping onto a set of nonlinear conductances [24].

Considering the effects of tunneling plasmons in the MIM heterojunction, we will show that at the plasmonic resonance, the effect of electric field localization occurring at the nanoantenna's feed gap may boost optical nonlinearities sourced from high-order quantum conductivities, thereby enabling efficient nonlinear optical rectification. We propose here the rigorous semiclassical modeling for an MIM metasurface with an ultrathin insulating layer at scales approaching the quantum limit. First, the Simmons' model is exploited to compute the dark tunneling current density of gap plasmons. Then, the Tien–Gordon theory [19] is used to calculate the second-order nonlinear conductivity induced by the photon-assisted tunneling process and predicts the photocurrent. Subsequently, the time-dependent current density can be expressed in the form of a Fourier series, giving rise to current densities at the fundamental frequency and harmonics, which in turn lead to various nonlinear optical and electro-optical effects associated with quantum conductivities.

Figure 1 illustrates the photon-assisted tunneling process in a dissimilar MIM junction formed by metals of different work functions, i.e., $\Phi_1 \neq \Phi_2$. The effective barrier height at the metal/insulator interface is $\varphi = \Phi - \chi$, where χ is the electron affinity of the insulator. In a general scenario, the voltage applied to the MIM structure is a combination of optical (ac) and dc signals. From the Tien–Gordon theory [19], the new time-dependent wavefunction for electrons in metal becomes

$$\psi(\bar{r}, t) = \psi_0(\bar{r}, t) \exp\left[-\frac{i}{\hbar}\int^{t} q\,V(t')\mathrm{d}t'\right] = \psi_0(\bar{r}, t)\sum_{n=-\infty}^{n=+\infty} J_n\left(\frac{q\,V_\omega}{\hbar\omega}\right) e^{-in\omega t}, \quad (1)$$

where q is the electron charge, $\hbar$ is the reduced Planck constant, $\psi_0(\bar{r}, t)$ is the unperturbed Schrödinger wavefunction, and $J_n(.)$ represents the nth order Bessel function. The modified wavefunction denotes that the monochromatic optical field adiabatically modulates the electron potential energy and excites new quantum-well virtual states separated from the unperturbed ground state by $\pm n\hbar\omega$, where n corresponds to the number of photons being absorbed or emitted by an electron on the metal surface, with a probability $J_n^2(q\,V_\omega/\hbar\omega)$ [25–27]. Subsequently, the time-dependent current is in the form of a Fourier series:

$$J(t) = \sum_{m=0}^{m=+\infty} \frac{1}{2}(J_{m\omega}e^{-im\omega t} + \text{c.c.}), \quad (2)$$

$$J_{\text{dc}} = \sum_{n=-\infty}^{\infty} J_0^2(q\,V_\omega/\hbar\omega)\,J_{\text{dark}}(q\,V_{\text{dc}} + n\hbar\omega), \quad (3)$$

$$J_{m\omega} = \sum_{n=-\infty}^{\infty} J_n(q\,V_\omega/\hbar\omega)[J_{n+m}(q\,V_\omega/\hbar\omega) + J_{n-m}(q\,V_\omega/\hbar\omega)] \times J_{\text{dark}}(q\,V_{\text{dc}} + n\hbar\omega), \quad (4)$$

where $\alpha = q\,V_\omega/\hbar\omega$, J_{dc}, and J_m are the dc ($m = 0$) and mth frequency-dependent currents. At infrared and visible wavelengths, $V_{\text{ph}} = \hbar\omega/q$, where the photon voltage is typically much higher than the electric voltage $V_\omega = \int \bar{E}_\omega \mathrm{d}l$, namely, if $\alpha \ll 1$, summations in Eqs. (3) and (4) can be simplified to [25,28,29]

$$J_\omega \approx \sigma_\omega^{(1)} E_\omega, \quad (5)$$

$$J_{\rm dc} \approx J_{\rm dark}(V_{\rm dc}) + \sigma_0^{(2)}|E_\omega|^2, \tag{6}$$

where the linear quantum conductivity $\sigma_\omega^{(1)}$ contributes to power dissipation inside the insulator, while the second-order quantum conductance $\sigma_0^{(2)}$ is responsible for the optical rectification, are given by

$$\sigma_\omega^{(1)} = \frac{qd}{\hbar\omega}\frac{J_{\rm dark}(V_{\rm dc}+\hbar\omega/q) - J_{\rm dark}(V_{\rm dc}-\hbar\omega/q)}{2}, \tag{7}$$

$$\sigma_0^{(2)} = \left(\frac{qd}{\hbar\omega}\right)^2 \times \frac{J_{\rm dark}(V_{\rm dc}+\hbar\omega/q) - 2J_{\rm dark}(V_{\rm dc}) + J_{\rm dark}(V_{\rm dc}-\hbar\omega/q)}{4}. \tag{8}$$

The tunneling dark current $J_{\rm dark}$ flowing between two dissimilar metal electrodes can be calculated using the well-known Simmons' theory [30]; Using Simmons' model, it can be shown that the tunneling current density is given by

$$J_{\rm dark}(V_{\rm dc}) = \frac{4\pi m_0 q}{h^3}\int_0^\infty D(\mathcal{E}_x)\mathrm{d}\mathcal{E}_x \times \int_{\mathcal{E}_x}^\infty [F_1(\mathcal{E}) - F_2(\mathcal{E}+qV_{dc})]\,\mathrm{d}\mathcal{E} \tag{9}$$

when a dc bias ($V_{\rm dc}$) is applied to the junction. m_0 and q denote the electronic charge and mass, respectively, whereas F_i represents the distribution of the Fermi–Dirac of the ith electrode, and h is Planck's constant. Finally, D denotes the transmission probability of electrons, $\mathcal{E}_x$ their longitudinal energy, and $\mathcal{E}$ their overall energy.

At equilibrium, the current–voltage characteristic is expressed by

$$J_{\rm dark}(V_{\rm dc}) = J_{1\to2} - J_{2\to1} = J_{{\rm dark},0}\left[\bar{\varphi}\exp(-A\sqrt{\bar{\varphi}}) - (\bar{\varphi}+qV_{\rm dc}) \times \exp\left(-A\sqrt{\bar{\varphi}+qV_{\rm dc}}\right)\right], \tag{10}$$

where $J_{{\rm dark},0} = q/2\pi h(\beta\Delta s)^2$, $J_{1\to2}$, and $J_{2\to1}$ represent the current density that flows from region 1 to region 2, and inversely, respectively. $A = 4\sqrt{2m_0}\pi\beta\Delta s/h$, and the correction factor is defined as $\beta = 1 - [1/(8\bar{\varphi}^2\Delta s)]\times\int_{s_1}^{s_2}[\varphi(x)-\bar{\Phi}]^2\mathrm{d}x$.

In the scenario of a reversed bias, the height of the tunneling barrier is given by

$$\varphi(x) = \varphi_1 + (\Delta\varphi - qV)\frac{x}{s} - \frac{q^2}{4\pi K\varepsilon_0 s}\left[\frac{x}{2} + \sum_{n=1}^{\infty}\frac{ns}{[(ns)^2-x^2]} - \frac{1}{ns}\right] \approx \varphi_1 + (\Delta\varphi - qV)\frac{x}{s} - 1.15\ln[2]\frac{q^2}{8\pi K\varepsilon_0}\frac{s}{x(s-x)}, \tag{11}$$

where s is the thickness of the tunnel barrier, $\Delta\varphi = \varphi_2 - \varphi_1 > 0$, and $\varphi_i = \Phi_i - \chi$ barrier height. Φ_i denotes the work function of the ith metal, and χ is the electron affinity of the insulating oxide. From Eq. (11), $\bar{\varphi}$ is given by

$$\bar{\varphi} = \frac{1}{\Delta s}\int_{s_1}^{s_2}\varphi(x)\mathrm{d}x \approx \varphi_1 + \frac{s_2+s_1}{2s}(\Delta\varphi - qV) - 1.15\ln[2]\frac{q^2}{8\pi K\varepsilon_0\Delta s}\ln\left[\frac{s_2(s-s_1)}{s_1(s-s_2)}\right]. \tag{12}$$

The parameters s_1 and s_2 are obtained by solving the following "cubic" equation:

$$\varphi_1 + (\Delta\varphi - qV)\frac{x}{s} - 1.15\ln[2]\frac{q^2}{8\pi K\varepsilon_0}\frac{s}{x(s-x)}. \tag{13}$$

From Eqs. (10), (12), and (13), one obtains the reverse-bias dark current density. In the forward-bias mode, $\bar{\varphi}$ is given by

$$\bar{\varphi} \approx \varphi_2 - \frac{s_2+s_1}{2s}(\Delta\varphi + qV) - 1.15\ln[2]\frac{q^2}{8\pi K\varepsilon_0\Delta s}\ln\left[\frac{s_2(s-s_1)}{s_1(s-s_2)}\right], \tag{14}$$

where s_1 and s_2 are again given by the real roots of

$$\varphi_2 + (\Delta\varphi + qV)\frac{x}{s} - 1.15\ln[2]\frac{q^2}{8\pi K\varepsilon_0}\frac{s}{x(s-x)}. \tag{15}$$

From Eqs. (10), (14), and (15), one obtains the forward-bias dark current density [21].

We note that in the infrared region and below the photoionization (internal photoemission) threshold, Eq. (3) is generally valid under the moderate irradiance, e.g., solar irradiance $\sim$0.1367 W/cm^2, and high-order nonlinearities responsible for multi-photon absorption and high-harmonic generations are generally negligible.

Figure 1(b) shows the spectrum of quantum conductivity $\sigma_\omega^{(1)}$ [S/m] and the zero-bias second-order quantum conductivity $\sigma_0^{(2)}$ [S/V] for an Ag-Nb_2O_5-Cu nanojunction. The work functions of Ag and Cu are $\Phi_1 = 4.26$ eV and $\Phi_2 = 4.7$ eV, and the thickness, the static relative permittivity, and the electron affinity of Nb_2O_5 are $t_{ox} = 2$ nm, $\kappa = 25$, and $\chi = 4$ eV [30–34], respectively. It is seen that at high photon energies, the values of $\sigma_\omega^{(1)}$ and $\sigma_0^{(2)}$ are higher than those predicted from the classic small-signal treatment (dashed lines), whereas both results are identical at long wavelengths. To quantify the optical-to-electrical conversion, the responsivity γ of the device can be expressed as

$$\gamma = \frac{\int\sigma_0^{(2)}|(\bar{E}_\omega\cdot\hat{z})|^2\mathrm{d}s}{\varepsilon_0 c\int|\bar{E}_{\rm inc}|^2\mathrm{d}s/2}, \tag{16}$$

where $\bar{E}_{\rm inc}$ is the electric field intensity of the incident light, $\bar{E}_\omega$ is the electric field intensity inside the insulating layer of MIM nanojunction (in general, $|E_\omega| > |E_{\rm inc}|$), and ε_0, and c are the permittivity and speed of light in free space [35–37].

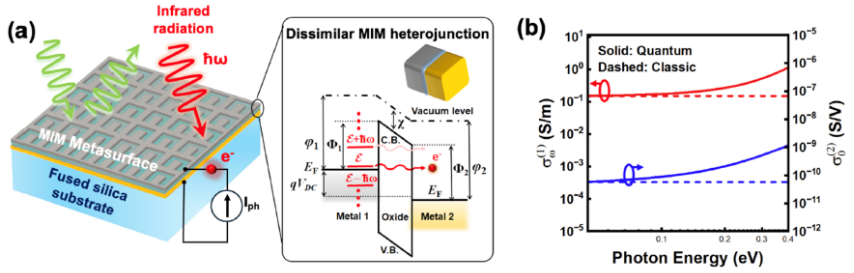

Fig. 1. (a) Schematic of an MIM metasurface used for mid-infrared detection. The inset shows the energy band diagram for photon-assisted tunneling occurring in a dissimilar MIM nanojunction; here, metal 1 and metal 2 have different work functions. (b) Linear and second-order quantum conductivities in an Ag-Nb_2O_5-Cu heterojunction with the insulator thickness $t_{ox} = 2$ nm.

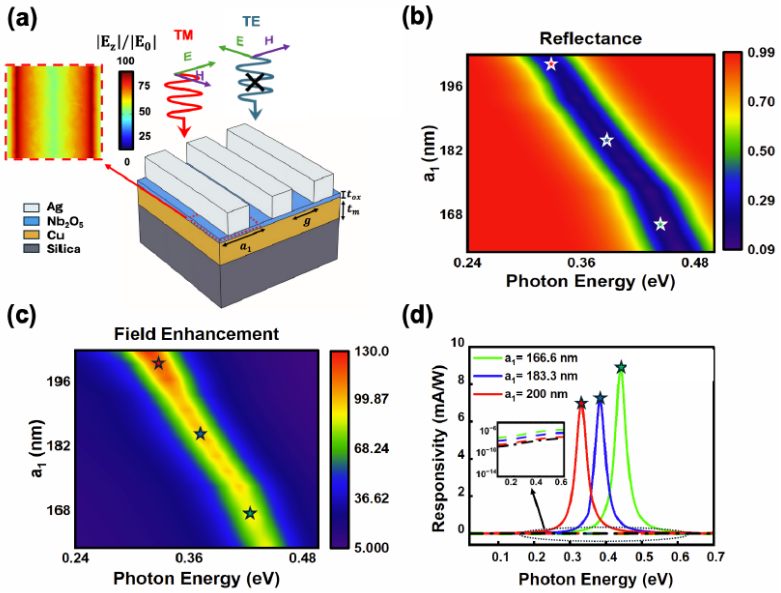

Fig. 2. (a) Schematic of the TM polarization-selective MIM photodetector; the inset shows the electric field in the insulator gap region. (b) Contours of reflectance as a function of period a_1 and photon energy for the MIM metasurface in (a); here, $g = 40$ nm. (c) is similar to (b), but for the field enhancement factor inside the insulator (Nb_2O_5). (d) Responsivity against photon energy for the MIM photodetector in (a) with different periods, which are illuminated by TM-polarized light (solid lines) and TE-polarized light (dashed lines); here, responsivity of an unpatterned MIM heterojunction (dash-dotted line) is also shown for comparison. The inset presents a zoom-in plot for the TE-polarized incident light (dashed lines) and the unpatterned MIM (dash-dotted line).

3. DESIGN AND ANALYSIS

A. Zero-Bias, Sub-Bandgap, Linear Polarization-Selective MIR Photodetection

Figure 2(a) shows the MIM metasurface-based zero-bias MIR photodetector, consisting of an Ag nanostrip array with a thickness of 50 nm, a 2 nm-thick Nb_2O_5 insulator, and a 50 nm-thick Cu thin film. The thickness of metallic layers was carefully chosen based on prior studies, as it must fall within a reasonable range that gives a favorable balance between optical confinement and plasmon losses [38,39]. The chosen metal thickness ensures sufficient structural continuity and strong field confinement while minimizing unwanted losses. The Ag nanostrip array has a gap $g = 40$ nm and lattice constant a_1. A fused silica layer is used as the substrate with a refractive index of 1.45. In our simulation, material properties fitted from experimental data were used for metals and dielectrics [40,41]. Figure 2(b) shows the contours of reflectance R as a function of photon energy and period a_1 for normally incident TM-polarized light. Figure 2(c) is similar to Fig. 2(b), but for the local field enhancement inside the Nb_2O_5 nanofilm; the field enhancement is defined as the average value of the z-component of electric field intensity in the insulator gap normalized by the incident electric field intensity. It can be seen when the resonant absorption occurs (which corresponds to the reflection dip in Fig. 2(b), as the absorptance $A = 1 - R$), large field enhancement can be

achieved in the Nb_2O_5 nanofilm, which, along with the perpendicular second-order quantum conductivity $\sigma_0^{(2)}$ induced inside the MIM heterojunction may result in detectable photocurrent, as known from Eq. (8). The reflectance and field enhancement were calculated using the finite-element frequency-domain method [40]. As can be seen in Figs. 2(b) and 2(c), the peak of absorption and its corresponding field enhancement can be tuned by altering the period of the metasurface, thus allowing spectral tunability for MIR photodetection. Moreover, this structure exhibits certain polarization selectivity, as it absorbs only the TM-polarized light, while reflecting most of the TE-polarized light. The inset of Fig. 2(a) shows the distribution of the electric field profile inside the Nb_2O_5 layer under the illumination of TM-polarized light. The field profile indicates strong localization of the electric field in the gap region of the MIM junction, which may enhance the light–matter interaction, critical for the optical rectification effect. Figure 2(d) reports the responsivity of MIM metasurface-based photodetectors highlighted by the asterisk in Fig. 2(c), under the illumination of both TE-polarized (dashed line) and TM-polarized (solid line) MIR radiation. By varying the period from 200 and 183.3 to 166.6 nm, the operating photon energy can be tuned from 0.44 and 0.38 to 0.33 eV, respectively; all devices exhibit a relatively narrowband operation with a bandwidth of ∼13% and a peak zero-bias responsivity greater than 7 mA/W. Also, it can be seen from Fig. 2(d) that this zero-bias MIR photodetector can be polarization-selective. Under the illumination of TE-polarized light, the peak responsivity is reduced to less than 6.45×10^{-6} mA/W. For the sake of comparison, a simple photodetector made of an unpatterned MIM nanojunction is also presented (dotted line; the responsivity is polarization-independent, with an average value of 4.3×10^{-8} mA/W in the spectral range of interest), showing that the metasurface structure plays a key role in effectively coupling light into the nonlinear nanojunction. The pronounced absorption observed for the TM-polarized incident light is attributed to the orientation of its electric field in relation to the periodic features of the structure. For the TM-polarized incident light, the in-plane electric field component is aligned with the direction of the grating to enable efficient coupling between the incident wave and resonant plasmonic modes supported inside the MIM structure. This coupling promotes the excitation of both localized and surface plasmon resonant modes. For TE-polarized incident light with the electric field perpendicular to gratings, much lower absorption is achieved due to the weakened modal coupling.

We note that the proposed device is CMOS-compatible. Unlike photodetectors based on InAsSb alloys [42], which need precise refractive index engineering, our MIM structure uses a much simpler and more fabrication-tolerant design, preventing the necessity for complex semiconductor processing. In addition, our structure enables resonance control over a wide spectral range by simply modifying the geometry of the metasurface. Unlike those quantum dot-based photodetectors [43], whose operating wavelength is primarily determined by material properties, the proposed zero-bias MIM metasurface-based photodetectors enable wideband tuning of the operating wavelength and polarization selectivity.

B. Zero-Bias, Sub-Bandgap, Circular Polarization-Selective MIR Photodetection

Figure 3(a) shows a zero-bias, circular polarization-selective MIR photodetector, whose device architecture is similar to that in Fig. 2(a) (i.e., Ag-Nb_2O_5-Cu heterojunction), but the Ag layer is patterned with a two-dimensional array of asymmetric slots to effectively couple circularly polarized light into the gap-plasmon region. The important geometric parameters are the width of the slot $w_2 = 35$ nm, the length of the slot $b_2 = 120$ nm, and the period a_2. We investigate the behavior of the structure for both right-hand circular polarization (RHCP) and left-hand circular polarization (LHCP). Through breaking the symmetry, this chiral structure can detect the rotation direction of circularly polarized light, as it selectively absorbs the RHCP light while reflecting the LHCP light. Figure 3(b) reports the contours of reflectance as a function of photon energy and period a_2, showing that the peak of resonant absorption can be tuned by varying the metasurface geometry such as period. Figure 3(c) is similar to Fig. 3(b), but for the contours of field enhancement. The maximum field intensity occurs at the photon energy of the absorption peak, which is tunable by modifying the metasurface geometry. The inset of Fig. 3(a) shows the electric field (E_z) distributions in the middle of the insulator layer under the illumination of the RHCP and LHCP light. It is evident that RHCP incident light is strongly confined and localized in the gap-plasmon region where the second-order nonlinearity is high. On the other hand, LHCP incident light is mostly reflected by the structure, resulting in weak field intensity within the nanojunction. The polarization selectivity in this design is due to the geometric chirality of the structure that breaks the mirror symmetry. This asymmetry gives rise to handedness-dependent coupling between the incident circularly polarized wave and the localized gap-plasmon mode in the MIM nanojunction. The orientation of unit cells on the metasurface in Fig. 3(a) matches the electric field rotation of RHCP light, enabling strong coupling and field localization within the gap region. The LHCP light, on the other hand, has a mismatch with the plasmonic mode, leading to destructive interference and suppressed coupling. Moreover, if the pattern were fabricated as the mirror image of the present geometry, the structure could sufficiently couple to LHCP light and reject RHCP light.

Figure 3(d) reports the zero-bias responsivity of circular polarization-selective MIR photodetectors highlighted by asterisks in Fig. 3(c), under the illumination of both RHCP (solid line) and LHCP radiation. As can be seen in Fig. 3(d), there is a drastic difference between the responsivities measured at different polarizations. For RHCP incident light, the operating photon energy can be readily tailored from 0.25 and 0.3 to 0.36 eV by reducing the period from 280 and 240 to 200 nm, respectively. Noticeably, the peak responsivity of all devices is greater than 2 mA/W. For LHCP incident light, the responsivity is as low as that of the unpatterned MIM nanojunction.

C. Wideband, Polarization-Insensitive MIR Photodetectors Based on the CSRR Metasurface

Figure 4(a) shows the wideband/dual-band, polarization-insensitive MIR photodetectors based on the same MIM

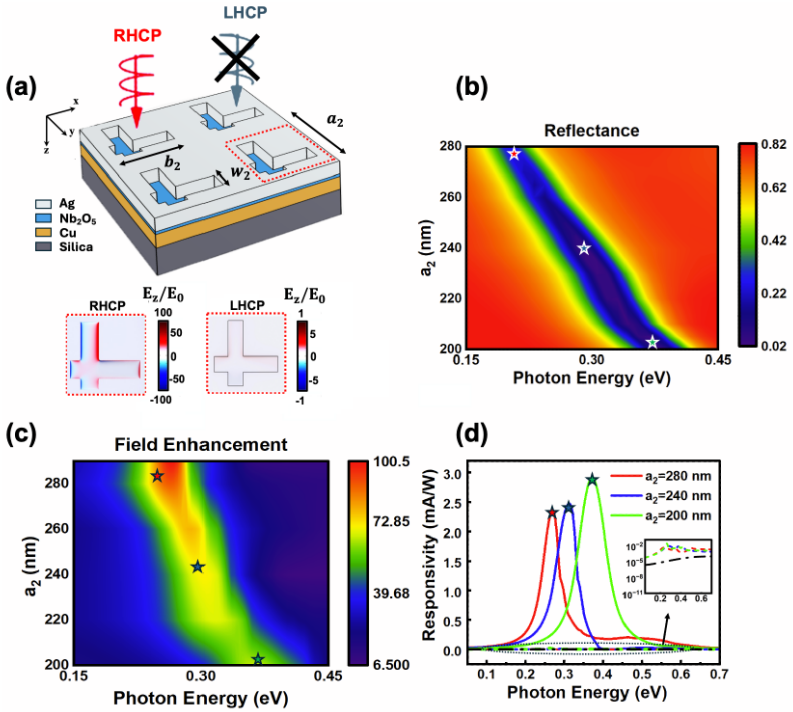

Fig. 3. (a) Schematic of the RHCP-selective MIM photodetector; the inset shows the electric field strength E_z in the middle of the insulating layer for both RHCP and LHCP. (b) Contours of reflectance as a function of period a_2 and photon energy for the structure in (a); here, $w_2 = 35$ nm and $b_2 = 120$ nm. (c) is similar to (b), but for the field enhancement factor inside the insulating layer. (d) Responsivity against photon energy for the photodetector in (a), illuminated by RHCP (solid lines) and LHCP (dashed lines) light; here, responsivity of an unpatterned MIM heterojunction (dash-dotted line) is also shown for comparison. The inset shows a zoom-in plot for LHCP incident light (dashed lines) and the unpatterned MIM (dash-dotted line).

plasmonic heterojunction in Fig. 2(a), but the Ag layer is patterned into a two-dimensional array of four-cut complementary split-ring resonators (CSRRs). The important geometric parameters of CSRR are the period $a_3 = 320$ nm, width and length of each L-shape slot, $w_3 = 70$ nm, $b_3 = 100$ nm, and gap size $c = 50$ nm. Figure 4(c) reports the contours of reflectance as a function of the photon energy and the length of the L-shape slot b_3. Figure 4(d) is similar to Fig. 4(c), but for the contours of field enhancement. It can be seen from Fig. 4(c) that the structure exhibits two resonant absorption peaks. The inset of Fig. 4(a) shows the electric field (E_z) distributions in the insulating layer of the MIM metasurface. The field distributions suggest that in this weakly coupled metasurface, the first and second resonant modes can be attributed to the electric dipole resonance and the electric quadrupole resonance, respectively. The first resonance occurring at the lower photon energy displays a dipole-like charge distribution, of which charges with opposite signs are accumulated on the adjacent arms of the split-ring resonator, forming a strong electric dipole moment that drives oscillating charges to produce a concentrated electric field within the insulating layer. The second resonance occurring at the higher photon energy displays a quadrupolar-like charge distribution, superimposing two electric dipoles of opposite orientation and strong field localization within the insulator layer. We further verified the physical origin of the two peaks by performing a multipole decomposition analysis [44,45]. Figure 4(b) shows the multipole decomposition for the structure in Fig. 4(a) with $b_3 = 120$ nm. The results confirm that the first peak is associated with the electric dipole, while the second peak is predominantly from the electric quadrupole. In this context, the corresponding modal coefficients are the induced multipole moments of the unit cell, namely the electric dipole (ED), magnetic dipole (MD), electric quadrupole (EQ), and magnetic quadrupole (MQ), which are extracted from the current distribution inside the unit cell and used as weighting factors in the decomposition of absorption spectra. Contributions from higher-order multipoles are found to be negligible and therefore not presented in Fig. 4(b).

The existence of multiple resonant absorption modes can effectively increase the spectral range of operation, provided that resonant modes are close to each other in the spectrum. Intuitively, multiband operation can be achieved when the two resonant modes are apart from each other. Figure 4(e) reports the responsivity of the polarization-independent CSRR metasurface-based photodetector sketched in Fig. 4(a), with different CSRR lengths (b_3). It can be seen that dual-band

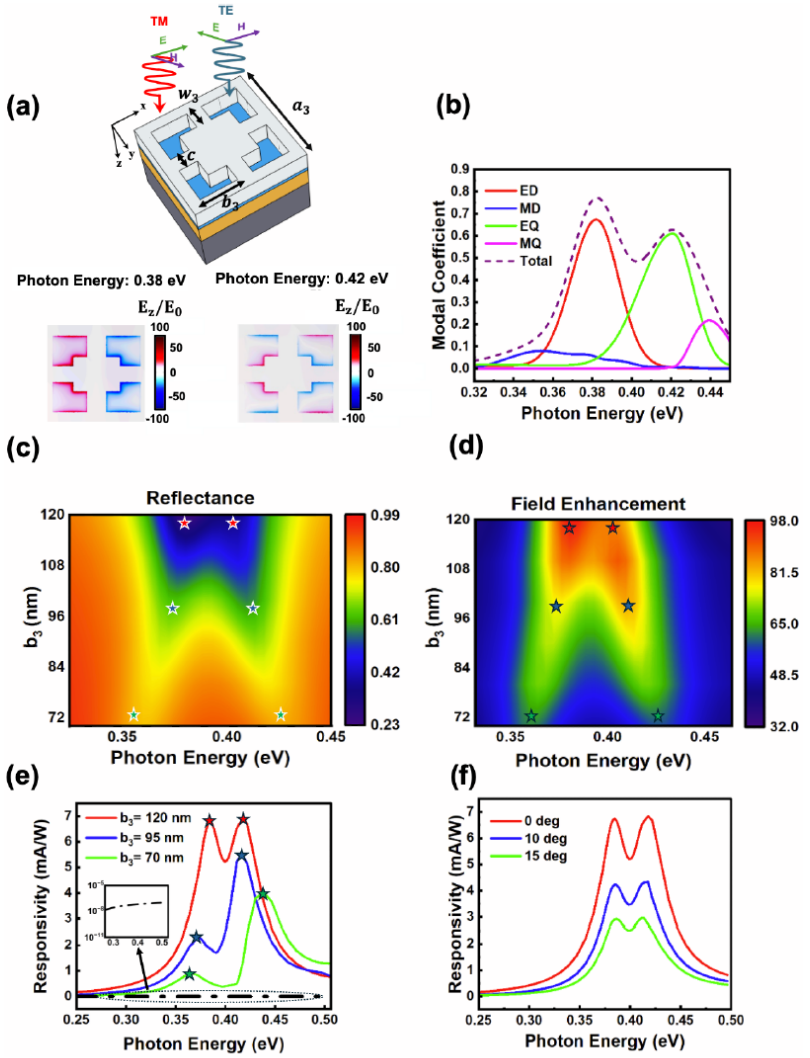

Fig. 4. (a) Schematic of the wideband MIM photodetector; the inset shows the electric field distributions (E_z) at the dipolar resonance (0.38 eV) and the quadrupolar resonance (0.42 eV). (b) Multipole decomposition for (a) the photodetector structure with $b_3 = 120$ nm. Contours of (c) reflectance and (d) field enhancement factor for the structure in (a), with $a_3 = 320$ nm, $w_3 = 70$ nm, $c = 50$ nm, and different values of b_3. (e) Responsivity against photon energy for the MIM photodetector in (a), with different values of b_3; here, responsivity of an unpatterned MIM heterojunction (dotted line) is also shown for comparison. The inset shows a zoom-in plot for the unpatterned MIM heterojunction (dash-dotted line). (f) Responsivity against photon energy for the photodetector in (a) for different values of the angle of incidence wave.

and wideband operations can be realized by tuning the geometric parameters of the CSRR–MIM metasurface. When $b_3 = 120$ nm, the zero-bias photodetector can have an average responsivity of 7 mA/W from 0.35 to 0.45 eV, with a ∼25% bandwidth of operation. This level of broadband responsivity is noteworthy given the compact, planar nature of the device. Moreover, we investigated the dependence of our structure on the angle of the incidence wave. Figure 4(f) shows the dependence of responsivity spectrum on angle of incidence. The results show by increasing the angle of incidence to 10° and 15°, the average responsivity decreases to 4 and 3 mA/W, respectively, while the spectral properties of the device remain nearly unchanged. Even though the responsivity level decreases at larger oblique incidence angles, The device can still operate at small incident wave angles, which shows the robustness of the device.

The proposed MIM photodetector structures can be fabricated using established nanofabrication techniques that can be employed for plasmonic and nano-optoelectronic devices. The metallic layers (Ag and Cu) can be deposited by methods such as

electron-beam evaporation or magnetron sputtering, ensuring smooth surfaces and accurate thickness control [46,47]. The ultrathin Nb_2O_5 insulator layer can be precisely grown with the atomic layer deposition technique [48] or the 2D template-assisted thermal synthesis method [49,50]. The pattern of metasurface, whether it is in the form of nanostrips, asymmetric slots, or CSRRs, can be formed by high-resolution electron-beam or focused-ion-beam lithography followed by the lift-off process [51]; current nanofabrication is capable of achieving feature sizes below 30 nm.

4. CONCLUSION

In summary, we have proposed and theoretically studied the MIM metasurface-based MIR photodetectors, which leverage the second-order quantum conductivity induced by tunneling plasmons in the dissimilar MIM heterojunction, alongside the large electric field enhancement within this plasmonic nanostructure, to achieve efficient optical rectification and photocurrent generation. Specifically, in this work, we have shown that by simply modifying the metasurface geometry, zero-bias, sub-bandgap, and spectrally/polarization-selective MIR photodetection can be realized, with responsivity at the mA/W scale. We envisage that the enhanced optical rectification, resulting from the interplay between the photon-assisted tunneling and the plasmon coupling within the nanoscale MIM metasurface, may offer great potential in the long-wavelength infrared detection for spectroscopy, thermal imaging, free-space optical communication, and low-power nanophotonic integrated circuits, as well as energy-harvesting devices (i.e., optical rectennas).

Funding. National Science Foundation (ECCS-2210977, ECCS-2210861).

Acknowledgment. PYC and ZZ would like to thank NSF Grant ECCS-2210977 and NSF Grant ECCS-2210861, respectively, for supporting the research reported in this publication.

Disclosures. The authors declare no conflicts of interest.

Data availability. The data that support the findings of this study are available from the corresponding author upon reasonable request.

REFERENCES

1. Y. Yao, A. Hoffman, and C. Gmachl, "Mid-infrared quantum cascade lasers," Nat. Photonics **6**, 432–439 (2012).
2. A. Rogalski, "Infrared detectors: an overview," Infrared Phys. **43**, 187–210 (2002).
3. L. Nordin, P. Petluru, A. Kamboj, *et al.*, "Ultra-thin all-epitaxial plasmonic detectors," Optica **8**, 1545–1551 (2021).
4. M. W. Knight, H. Sobhani, P. Nordlander, *et al.*, "Photodetection with active optical antennas," Science **332**, 702–704 (2011).
5. N. Vu, P. Heidarzadeh, and P.-Y. Chen, "Plasmonic metagrating-interlayer semiconductor (PMIS) structure for enhancing photodetection via hot-electron injection," Opt. Express **32**, 33974–33983 (2024).
6. W. Li and J. Valentine, "Metamaterial perfect absorber based hot electron photodetection," Nano Lett. **14**, 3510–3514 (2014).
7. P.-Y. Chen, M. Hajizadegan, M. Sakhdari, *et al.*, "Giant photoresponsivity of midinfrared hyperbolic metamaterials in the photon-assisted-tunneling regime," Phys. Rev. Appl. **5**, 041001 (2016).
8. A. B. Hoofring, V. J. Kapoor, and W. Krawczonek, "Submicron nickel-oxide-gold tunnel diode detectors for rectennas," J. Appl. Phys. **66**, 430–437 (1989).
9. Y. Cui, K. H. Fung, J. Xu, *et al.*, "Ultrabroadband light absorption by a sawtooth anisotropic metamaterial slab," Nano Lett. **12**, 1443–1447 (2012).
10. J. Shen, T. Zhu, J. Zhou, *et al.*, "High-discrimination circular polarization detection based on dielectric-metal-hybrid chiral metamirror integrated quantum well infrared photodetectors," Sensors **23**, 168 (2022).
11. P.-Y. Chen, R. Salas, and M. Farhat, "Generation of high-power terahertz radiation by nonlinear photon-assisted tunneling transport in plasmonic metamaterials," J. Opt. **19**, 124012 (2017).
12. I. McGregor and K. M. Hock, "Complementary split-ring resonator-based deflecting structure," Phys. Rev. Accel. Beams **16**, 090101 (2013).
13. X. Gao, L. Zhou, and T. J. Cui, "Odd-mode surface plasmon polaritons supported by complementary plasmonic metamaterial," Sci. Rep. **5**, 9250 (2015).
14. S. A. Maier, *Plasmonics: Fundamentals and Applications* (Springer, 2007).
15. G. Dayal, I. Morichika, and S. Ashihara, "Vibrational strong coupling in subwavelength nanogap patch antenna at the single resonator level," J. Phys. Chem. Lett. **12**, 3171–3175 (2021).
16. J. Lee, M. Tymchenko, C. Argyropoulos, *et al.*, "Giant nonlinear response from plasmonic metasurfaces coupled to intersubband transitions," Nature **511**, 65–69 (2014).
17. P.-Y. Chen, C. Argyropoulos, G. D'Aguanno, *et al.*, "Enhanced second-harmonic generation by metasurface nanomixer and nanocavity," ACS Photonics **2**, 1000–1006 (2015).
18. J. Lee, S. Jung, P.-Y. Chen, *et al.*, "Ultrafast electrically tunable polaritonic metasurfaces," Adv. Opt. Mater. **2**, 1057–1063 (2014).
19. P. K. Tien and J. P. Gordon, "Multiphoton process observed in the interaction of microwave fields with the tunneling between superconductor films," Phys. Rev. **129**, 647 (1963).
20. J. Lee, Y. Wu, I. Sinev, *et al.*, "Plasmonic biosensor enabled by resonant quantum tunnelling," Nat. Photonics **19**, 938–945 (2025).
21. M. Farhat, M. M. Cheng, K. Q. Le, *et al.*, "Nanoantenna harmonic sensor: theoretical analysis of contactless detection of molecules with light," Nanotechnology **26**, 415201 (2015).
22. K. J. Savage, M. M. Hawkeye, R. Esteban, *et al.*, "Revealing the quantum regime in tunnelling plasmonics," Nature **491**, 574–577 (2012).
23. B. Lovász, P. Sándor, G. Z. Kiss, *et al.*, "Nonadiabatic nano-optical tunneling of photoelectrons in plasmonic near-fields," Nano Lett. **22**, 2303–2308 (2022).
24. P. S. Davids and J. Shank, "Density matrix approach to photon-assisted tunneling in the transfer Hamiltonian formalism," Phys. Rev. B **97**, 075411 (2018).
25. J. W. Haus, D. de Ceglia, M. A. Vincenti, *et al.*, "Quantum conductivity for metal–insulator–metal nanostructures," J. Opt. Soc. Am. B **31**, 259–269 (2014).
26. P.-Y. Chen, M. Farhat, and H. Bağcı, "Graphene metascreen for designing compact infrared absorbers with enhanced bandwidth," Nanotechnology **26**, 164002 (2015).
27. J. R. Tucker, "Quantum limited detection in tunnel junction mixers," IEEE J. Quantum Electron. **15**, 1234–1258 (1979).
28. J. Haus, D. de Ceglia, M. Vincenti, *et al.*, "Nonlinear quantum tunneling effects in nanoplasmonic environments: two-photon absorption and harmonic generation," J. Opt. Soc. Am. B **31**, A13–A19 (2014).
29. P.-Y. Chen and M. Farhat, "Modulatable optical radiators and metasurfaces based on quantum nanoantennas," Phys. Rev. B **91**, 035426 (2015).
30. J. G. Simmons, "Generalized formula for the electric tunnel effect between similar electrodes separated by a thin insulating film," J. Appl. Phys. **34**, 1793–1803 (1963).
31. N. Alimardani and J. F. Conley, "Enhancing metal-insulator-insulator-metal tunnel diodes via defect enhanced direct tunneling," Appl. Phys. Lett. **105**, 082902 (2014).
32. N. Alimardani, S. W. King, B. L. French, *et al.*, "Investigation of the impact of insulator material on the performance of dissimilar electrode metal-insulator-metal diodes," J. Appl. Phys. **116**, 024508 (2014).

33. E. W. Cowell, N. Alimardani, C. C. Knutson, *et al.*, "Advancing MIM electronics: amorphous metal electrodes," Adv. Mater. **23**, 74–78 (2011).
34. S. Grover and G. Moddel, "Engineering the current–voltage characteristics of metal–insulator–metal diodes using double-insulator tunnel barriers," Solid State Electron. **67**, 94–99 (2012).
35. P.-Y. Chen and A. Alù, "Optical nanoantenna arrays loaded with nonlinear materials," Phys. Rev. B **82**, 235405 (2010).
36. P.-Y. Chen and A. Alù, "Subwavelength imaging using phase-conjugating nonlinear nanoantenna arrays," Nano Lett. **11**, 5514–5518 (2011).
37. P. Y. Chen, M. Farhat, and A. Alù, "Bistable and self-tunable negative-index metamaterial at optical frequencies," Phys. Rev. Lett. **106**, 105503 (2011).
38. X. Hu, F. Li, H. Wu, *et al.*, "Suppression of gap plasmon resonance for high-responsivity metal–insulator–metal near-infrared hot-electron photodetectors," Opt. Lett. **47**, 42–45 (2021).
39. Z. Sakotic, A. Raju, A. Ware, *et al.*, "Mid-infrared perfect absorption with planar and subwavelength-perforated ultrathin metal films," Adv. Phys. Res. **3**, 2400012 (2024).
40. "COMSOL Multiphysics v. 6.0," COMSOL AB, 2022, https://www.comsol.com.
41. L. Gao, F. Lemarchand, and M. Lequime, "Comparison of different dispersion models for single layer optical thin film index determination," Thin Solid Films **520**, 501–509 (2011).
42. N. C. Mansfield, Y. Tischenko, M. Bergthold, *et al.*, "Room temperature mid-wave infrared guided mode resonance InAsSb photodetectors," Appl. Phys. Lett. **125**, 171107 (2024).
43. M. Malerba, M. Jeannin, S. Pirotta, *et al.*, "A "Janus" double sided mid-IR photodetector based on a MIM architecture," Appl. Phys. Lett. **119**, 181102 (2021).
44. R. Dezert, P. Richetti, and A. Baron, "Complete multipolar description of reflection and transmission across a metasurface for perfect absorption of light," Opt. Express **27**, 26317–26330 (2019).
45. H. K. Shamkhi, A. Sayanskiy, A. C. Valero, *et al.*, "Transparency and perfect absorption of all-dielectric resonant metasurfaces governed by the transverse Kerker effect," Phys. Rev. Mater. **3**, 085201 (2019).
46. Z. Wang and Z. Zhang, "Electron beam evaporation deposition," in *Advanced Nano Deposition Methods* (Wiley, 2016), pp. 33–58.
47. M. Hu, X. Gao, L. Weng, *et al.*, "The microstructure and improved mechanical properties of Ag/Cu nanoscaled multilayer films deposited by magnetron sputtering," Appl. Surf. Sci. **313**, 563–568 (2014).
48. M. Leskelä and M. Ritala, "Atomic layer deposition chemistry: recent developments and future challenges," Angew. Chem. Int. Ed. Engl. **42**, 5548–5554 (2003).
49. Q. Cui, M. Sakhdari, B. Chamlagain, *et al.*, "Ultrathin and atomically flat transition-metal oxide: promising building blocks for metal–insulator electronics," ACS Appl. Mater. Interfaces **8**, 34552–34558 (2016).
50. B. Chamlagain, Q. Cui, S. Paudel, *et al.*, "Thermally oxidized 2D TaS_2 as a high-κ gate dielectric for MoS_2 field-effect transistors," 2D Mater. **4**, 031002 (2017).
51. W. Cai and V. Shalaev, *Optical Metamaterials* (Springer, 2010).